



# Blade Heat Transfer Measurements and Predictions in a Transonic Turbine Cascade

P.W. Giel  
Dynacs Engineering Company, Inc., Cleveland, Ohio

G.J. Van Fossen and R.J. Boyle  
Glenn Research Center, Cleveland, Ohio

D.R. Thurman and K.C. Civinskas  
U.S. Army Research Laboratory, Glenn Research Center, Cleveland, Ohio

## The NASA STI Program Office . . . in Profile

Since its founding, NASA has been dedicated to the advancement of aeronautics and space science. The NASA Scientific and Technical Information (STI) Program Office plays a key part in helping NASA maintain this important role.

The NASA STI Program Office is operated by Langley Research Center, the Lead Center for NASA's scientific and technical information. The NASA STI Program Office provides access to the NASA STI Database, the largest collection of aeronautical and space science STI in the world. The Program Office is also NASA's institutional mechanism for disseminating the results of its research and development activities. These results are published by NASA in the NASA STI Report Series, which includes the following report types:

- **TECHNICAL PUBLICATION.** Reports of completed research or a major significant phase of research that present the results of NASA programs and include extensive data or theoretical analysis. Includes compilations of significant scientific and technical data and information deemed to be of continuing reference value. NASA's counterpart of peer-reviewed formal professional papers but has less stringent limitations on manuscript length and extent of graphic presentations.
- **TECHNICAL MEMORANDUM.** Scientific and technical findings that are preliminary or of specialized interest, e.g., quick release reports, working papers, and bibliographies that contain minimal annotation. Does not contain extensive analysis.
- **CONTRACTOR REPORT.** Scientific and technical findings by NASA-sponsored contractors and grantees.

- **CONFERENCE PUBLICATION.** Collected papers from scientific and technical conferences, symposia, seminars, or other meetings sponsored or cosponsored by NASA.
- **SPECIAL PUBLICATION.** Scientific, technical, or historical information from NASA programs, projects, and missions, often concerned with subjects having substantial public interest.
- **TECHNICAL TRANSLATION.** English-language translations of foreign scientific and technical material pertinent to NASA's mission.

Specialized services that complement the STI Program Office's diverse offerings include creating custom thesauri, building customized data bases, organizing and publishing research results . . . even providing videos.

For more information about the NASA STI Program Office, see the following:

- Access the NASA STI Program Home Page at <http://www.sti.nasa.gov>
- E-mail your question via the Internet to [help@sti.nasa.gov](mailto:help@sti.nasa.gov)
- Fax your question to the NASA Access Help Desk at (301) 621-0134
- Telephone the NASA Access Help Desk at (301) 621-0390
- Write to:  
NASA Access Help Desk  
NASA Center for Aerospace Information  
7121 Standard Drive  
Hanover, MD 21076



# Blade Heat Transfer Measurements and Predictions in a Transonic Turbine Cascade

P.W. Giel  
Dynacs Engineering Company, Inc., Cleveland, Ohio

G.J. Van Fossen and R.J. Boyle  
Glenn Research Center, Cleveland, Ohio

D.R. Thurman and K.C. Civinskas  
U.S. Army Research Laboratory, Glenn Research Center, Cleveland, Ohio

Prepared for the  
1999 International Gas Turbine and Aeroengine Congress  
cosponsored by the American Society of Mechanical Engineers and  
the International Gas Turbine Institute  
Indianapolis, Indiana, June 7-10, 1999

National Aeronautics and  
Space Administration

Glenn Research Center

## Acknowledgments

This work was supported by the NASA Glenn Research Center under contract NAS3-98008 with Dynacs Engineering Co., Inc., with Mr. Robert J. Boyle as monitor. The support of Ms. Mary Ann Johnston in digitizing the data and of Mr. James Fellenstein and Ms. Margaret Proctor in measuring the surface roughness is also gratefully acknowledged.

### Available from

NASA Center for Aerospace Information  
7121 Standard Drive  
Hanover, MD 21076  
Price Code: A03

National Technical Information Service  
5285 Port Royal Road  
Springfield, VA 22100  
Price Code: A03

# Blade Heat Transfer Measurements and Predictions in a Transonic Turbine Cascade

P. W. Giel

Dynacs Engineering Company, Inc.  
Brook Park, OH 44142

G. J. Van Fossen, R. J. Boyle

NASA Glenn Research Center  
Cleveland, OH 44135

D. R. Thurman and K. C. Civinskas

U.S. Army Research Laboratory / Vehicle Technology Center  
NASA Glenn Research Center  
Cleveland, OH 44135

## ABSTRACT

Detailed heat transfer measurements and predictions are given for a turbine rotor with 136° of turning and an axial chord of 12.7 cm. Data were obtained for inlet Reynolds numbers of 0.5 and  $1.0 \times 10^6$ , for isentropic exit Mach numbers of 1.0 and 1.3, and for inlet turbulence intensities of 0.25% and 7.0%. Measurements were made in a linear cascade having a highly three-dimensional flow field resulting from thick inlet boundary layers. The purpose of the work is to provide benchmark quality data for three-dimensional CFD code and model verification. Data were obtained by a steady-state technique using a heated, isothermal blade. Heat fluxes were determined from a calibrated resistance layer in conjunction with a surface temperature measured by calibrated liquid crystals. The results show the effects of strong secondary vortical flows, laminar-to-turbulent transition, shock impingement, and increased inlet turbulence on the surface heat transfer.

## LIST OF SYMBOLS

$C_p$  - specific heat [J/kg·K]  
 $C_x$  - blade axial chord [cm]  
 $d$  - rotor leading edge diameter [cm]  
 $k$  - thermal conductivity [W/m·K]  
 $k^+$  - equivalent roughness height  
 $L_r$  - longitudinal integral turbulence length scale [cm]  
 $M$  - Mach number  
 $P$  - pressure [Pa]  
 $Pr$  - Prandtl number

$q''$  - heat flux [W/m<sup>2</sup>]  
 $r$  - recovery factor,  $r = Pr^{1/3}$   
 $Re_{in}$  - Reynolds number,  $Re_{in} = \rho U_{in} C_x / \mu$   
 $s$  - blade surface coordinate [cm]  
 $St$  - Stanton number  
 $t$  - thickness [cm]  
 $T$  - temperature [K]  
 $Tu$  - turbulence intensity  
 $U$  - total velocity [m/s]  
 $y^+$  - equivalent normal distance  
 $z$  - spanwise (radial) coordinate  
 $\gamma$  - specific heat ratio,  $\gamma = 1.4$   
 $\delta$  - 99% boundary layer thickness [cm]  
 $\epsilon$  - emissivity  
 $\theta$  - nondimensional surface temperature  
 $= (T_{lc} - T_{aw}) / (T_{cu} - T_{lc})$   
 $\mu$  - dynamic viscosity [kg/s·m]  
 $\mu_t$  - turbulent eddy viscosity [kg/s·m]  
 $\rho$  - density [kg/m<sup>3</sup>]  
 $\sigma$  - Stefan-Boltzmann constant

Subscripts

$aw$  - adiabatic wall temperature  
 $cu$  - copper substrate  
 $lc$  - liquid crystal  
 $ex$  - exit freestream value  
 $in$  - inlet freestream value  
 $IS$  - isentropic value

Superscripts

$t$  - total conditions

## INTRODUCTION

Highly detailed heat transfer data at conditions approximating those in actual engines are needed to verify computational fluid dynamic (CFD) predictive analyses. Accurate local heat transfer predictions are required to improve blade service life and to reduce cooling requirements. Accurate heat transfer measurements for CFD verification require the good spatial resolution of a large-scale facility. The large scale, combined with high Reynolds and Mach numbers, in turn requires high mass flow rates per passage. A linear cascade, with fewer blades than a full annular cascade, provides better spatial resolution for the same overall flow rate. Previous studies have shown that rotor geometries in linear cascades provide good midspan data as compared to their rotating equivalents. See, for example, Baughn et al. (1995) or Guenette et al. (1989). Also, Graziani et al. (1980) studied the effects of thick and thin endwall boundary layers on rotor heat transfer in a low speed linear cascade. Blair (1994) measured heat transfer in a low speed facility on a rotating blade that had the same midspan section as the blade of Graziani et al. (1980). Similar three-dimensional heat transfer patterns were observed at and below midspan of those two tests. Linear cascades can and have also been used to study tip clearance heat transfer, but the current study emphasizes blade data away from the tip region.

Although many turbine applications use film cooling for blade temperature control, data without film cooling are needed to validate predictions of heat transfer coefficients. With film cooling present, differences between the analysis and data could be due to differences in either heat transfer coefficients or in the film effectiveness distribution. Transition influences blade heat transfer, while endwall flows are more likely to be turbulent. Transition is not an issue in film cooled blades, where the film cooling trips the flow to turbulent. However, it is important to accurately predict transition, both for heat transfer on a non-film cooled blade, and for the aerodynamics of the low pressure turbine where heat transfer data can be used to verify transition predictions. Secondary flow effects on heat transfer differ between the blade and endwall.

Aerodynamic and heat transfer data are needed at the same flow conditions to thoroughly understand the flow physics. The objective of the current study is to provide a detailed, high Mach number rotor blade heat transfer data set to CFD code developers and users so that they can better manage the uncertainty associated with heat transfer predictions. The current study, along with the aerodynamic study (Giel et al., 1996a), and the endwall heat transfer study (Giel et al., 1998), provide a complete and detailed data set for CFD code and model validation. A baseline 3-D CFD analysis is included to illustrate where improved modeling is needed.

Along with the studies mentioned above, detailed measurements were reported by Goldstein and Spores (1988) and Goldstein et al. (1995) for rotors in large scale low speed linear cascades. These studies used a naphthalene sublimation technique while Graziani et al. (1980) used heated blade and endwall surfaces. Dunn et al. (1994) measured rotor heat transfer at discrete chordwise and spanwise locations in a shock tube facility at engine-typical gas-to-wall temperature ratios and Mach numbers. These measurements were on engine-size hardware using heat flux gauges. Consequently, the resolution was less than for the large scale facility measurements. Martinez-Botas et al. (1994) used a liquid crystal technique to measure heat transfer for an uncooled stator in a blowdown annular cascade at transonic conditions.

The NASA Glenn Research Center Transonic Turbine Blade Cascade provides heat transfer and aerodynamic data to verify CFD analyses. Data were obtained for eight different flow conditions, and illustrate the effects of varying Reynolds number, exit Mach number, and inlet turbulence. Measurements were made at inlet Reynolds numbers of 0.5 and  $1.0 \times 10^6$ , and exit pressures corresponding to isentropic Mach numbers of 1.0 and 1.3. Tests were conducted at high and low inlet turbulence levels. Twelve blades ensured good periodicity. The axial chord was 12.7 cm. The Reynolds and Mach numbers are relevant to high pressure turbines where heat transfer is critical. Results herein show the effects of shock/boundary layer interactions and of longitudinal vortices on blade heat transfer, which become more significant as Mach numbers and flow turning increase.

The rotor, of constant cross section, is highly loaded with 136 degrees of turning, and an inlet flow angle of 63.6 degrees. The cascade geometry is two-dimensional, but the flows are highly three-dimensional due to thick boundary layers developed on the long cascade inlet. Each boundary layer was one-third of the half-span. The full span-to-axial chord ratio was 1.2. The thick boundary layers and high flow turning resulted in spanwise flow variations as large as those seen in rotating turbines. See, for example, Joslyn and Dring (1992) or Thulin et al. (1982). These variations result from secondary flows, and accurately predicting them is a significant test of a three-dimensional analysis. Tests were done with and without a blown, square bar grid upstream of the blade row.

Using liquid crystals to measure heat transfer gave good spatial resolution. Several versions of liquid crystal measurement techniques have been used for gas turbine related measurements. A transient technique was used by Martinez-Botas et al. (1994), and a steady-state technique was used by Hippensteele et al. (1985). The roughness of the liquid crystals is documented because of its heat transfer importance.

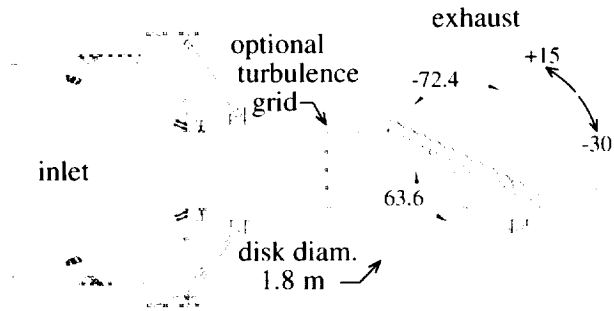


**Fig. 1 Transonic Turbine Blade Cascade**

Rotor shape was influenced by both aerodynamic and heat transfer considerations. Predicted rotor profile loss was consistent with current design practice. Arts et al. (1997), Dunn et al. (1994), and Blair (1994) among others, showed midspan rotor blade leading edge heat transfer rates nearly twice the highest values seen elsewhere on the blade. Civinskas et al. (1990) showed heat transfer in this region was reduced using a large leading edge diameter, and aerodynamic losses were not significantly increased. The rotor shape was chosen to achieve acceptable aerodynamics with a lower than typical ratio of peak-to-average heat transfer. This lower peak-to-average heat transfer had a secondary benefit in that measuring heat transfer over a narrower range inherently reduces experimental uncertainty.

### DESCRIPTION OF FACILITY

**Cascade Description** An initial facility description was given by Verhoff et al. (1992). The cascade inlet section was analyzed and redesigned (Giel et al. 1996b) to improve inlet flow pitchwise uniformity. Figure 1 shows an overall view of the redesigned facility. Passage 1 is at the upper left and passage 11 is at the lower right.

High pressure, ambient temperature air was throttled to an inlet total pressure near one atmosphere for the high Reynolds number tests. Low Reynolds number tests had an inlet total pressure near one-half atmosphere. The air discharged into an exhaust header maintained at a nominal pressure of 15.9 kPa (2.3 psia). A valve between the test section and exhaust header was used to maintain the desired exit Mach number. Figure 1 shows the test section mounted on a large disk, which can rotate to vary inlet incidence angle. Results herein were obtained at the design inlet flow angle of 63.6 degrees. Upstream inlet boards were used, but to minimize downstream shock reflections no exit tailboards were used. Thick boundary layers developed in the long inlet section. Aerodynamic probe and blade loading data verified the existence of strongly three-dimensional passage flow.

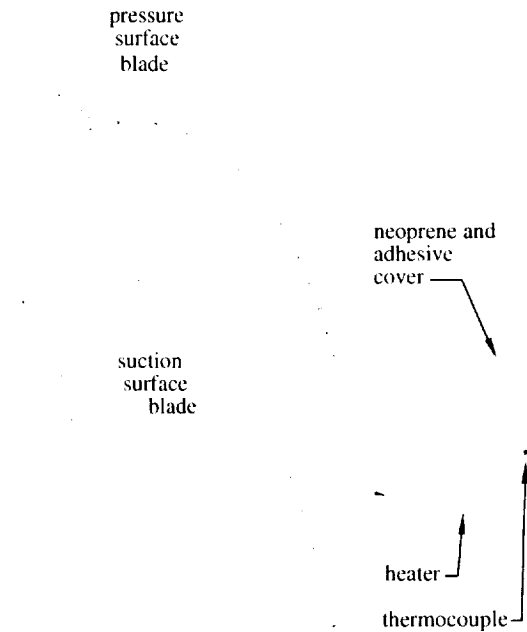


**Fig. 2 Heat Transfer Measurement Blades**

**Table 1 Blade and cascade parameters and dimensions**

Geometric parameter	Value
axial chord	12.70 cm (5.000 inches)
pitch	13.00 cm (5.119 inches)
span	15.24 cm (6.000 inches)
true chord	18.42 cm (7.250 inches)
stagger angle	41.54°
throat dimension	3.358 cm (1.393 inches)
throat area: 1 passage	53.94 cm <sup>2</sup>
leading edge diameter	2.657 cm (1.046 inches)
trailing edge diameter	0.518 cm (0.204 inches)
turbulence grid	2.54 cm square bar
Flow parameter	Value
Inlet Reynolds No.	$0.5 \times 10^6$ or $1.0 \times 10^6$
Exit Reynolds No.	$0.9 \times 10^6$ or $1.8 \times 10^6$
Inlet Mach No., $M_{IS}$	0.38
Exit Mach No., $M_{IS}$	1.32 or 0.98
Inlet $\delta$ - no grid	3.2 cm (1.2 inch)
with grid	2.0 cm (0.8 inch)
Inlet flow angle	63.6°
Design flow turning	136°

Blade and cascade details are given in Table 1. The two blades forming passage 5 were instrumented; one for the suction surface and one for the pressure surface with some leading edge overlap. Both endwalls were 6.35 cm (2.50 in.) thick clear acrylic for optical access.

### Measurement Blade Description

High strength metal blades were fabricated from high-conductivity, oxygen-free copper to withstand large pressure differentials due to high exit Mach numbers. They were undercut by 0.66 mm (0.026 in.) to accommodate a composite low thermal conductivity layer across which heat transfer rates were measured. Figure 2 shows the layer to be 0.15 mm (0.006 in.) of double-faced adhesive film and 0.51 mm (0.020 in.) of neoprene rubber. Liquid crystals were sprayed on the outer surface. The adhesive film and the neoprene rubber were rolled carefully onto the copper surface. The following transient tests were performed to verify uniform bonding of both: A heat gun was used to quickly heat the surface until the liquid crystal yellow line was visible. The surface was then allowed to cool. Any regions with air bubbles trapped in the composite layer responded more slowly to the transient heating and cooling and thus appeared as obvious distortions in the yellow line. The layer in this region was then punctured with a fine hypodermic needle to eliminate the bubble. In another test, the blade heaters were turned on abruptly while the test section was under a vacuum. A spanwise liquid crystal yellow line was observed to move from the thinner sections of the blade slowly towards the thicker sections. The two-dimensionality of this line further verified uniform composite layer bonding.

Cylindrical electrical cartridge heaters extended the entire span of the blades just under the surface. They were positioned to maintain copper temperature uniformity within 0.15°C (0.25°F). Sheathed Type E 0.51 mm (0.020 in.) thermocouples, in copper surface grooves, were used by feedback control circuits and a D.C. power supply to maintain the copper substrate at a uniform temperature. For most flow conditions the midspan copper thermocouple temperatures were maintained to within ±0.6°C (±1°F). An additional row of thermocouples at the same surface distances as the midspan row was located 6.4 mm (0.25 in.) from the endwall nearest the cameras. The four thermocouples surrounding any point on the blade were used in a bilinear ( $s, z$ ) interpolation procedure. This interpolation gave the local  $T_{c,u}$  and thus the local heat flux at any surface location, eliminating the need to correct for endwall heat loss.

The composite layer conductance,  $k/t$ , was calibrated in a separate test. A small rectangular test plate was made of the same copper material and was instrumented with the same thermocouples, adhesive film, neoprene rubber, and liquid crystals that were used in the blade tests. A thin-film electrical heater was bonded to the bottom surface and the current and voltage were carefully monitored to determine the heat flux through the plate. Thermal insulation, thermocouples, and guard heaters were placed on the bottom surface and around

all four edges. Compressed air was blown on the surface at various flow rates to in order to vary the external heat transfer coefficient. At each blowing rate, the heater power was adjusted until the liquid crystal yellow line was visible. The conductance was then calculated from the heat flux and the temperature difference between the copper substrate and the liquid crystals. The composite layer conductance,  $k/t$ , was calibrated as 468 W/m<sup>2</sup>·K, ±5% (82.5 BTU/hr·ft<sup>2</sup>·R) and was not found to vary significantly over the range of heat fluxes tested. The heat transfer measurement technique was first tested on a circular cylinder in cross-flow, and results agreed with well-established data.

A profilometer measured several 5-mm traces after the liquid crystals were sprayed on. A 60× photomicrograph showed that the profilometer stylus did not alter the crystals. The arithmetic mean roughness was 6.5 μm and the r.m.s. roughness was 7.8 μm. The average spatial frequency of roughness was 10.4 mm<sup>-1</sup> so the average peak-to-peak distance was 0.097 mm. The equivalent roughness height was estimated to be 7 μm. The maximum normalized roughness height,  $k^+$ , was estimated to be 3.5, so from a surface roughness standpoint the blade surface was hydraulically smooth. More details of the surface characteristics including digitized traces and surface FFT's are available from the authors.

### Turbulence Grid Description

A 74% open area square bar turbulence grid, 6.9  $C_x$ , upstream of the measurement passage, positioned normal to the inlet flow, was used for some tests (see Fig. 1). Square 25 mm (1 in.) tubes, one extending between the inlet boards at midspan, interconnected to three spanwise tubes located on 150 mm centers formed the grid. Balanced air at 965 kPa (125 psig) entered the entire grid through both ends of the spanwise tubes, and exited upstream through 75 3.2 mm (1/8 inch) diameter holes. The holes were spaced uniformly on 12.7 mm (1/2 inch) centers with 11 on each spanwise tube and 42 on the tube extending between the inlet boards. Each row of holes was centered on its respective square tube. The flow from each hole directly opposed the mainstream flow. Total mass flow from the grid was 0.65 kg/s (1.4 lb<sub>m</sub>/s) for all cases, corresponding to 5% of the cascade mass flow at  $Re_{in} = 1.0 \times 10^6$ . This grid was used in a previous end-wall heat transfer study (see Giel et al., 1998), but with no grid air. Boyle et al. (1998a) showed that upstream blowing produced a more uniform mean and fluctuating flow field compared to an unblown grid.

## MEASUREMENT TECHNIQUES

### Inlet Flow Measurements

Aerodynamic probe measurements were made on a plane one axial chord upstream of the blade leading edge plane. In the pitch-

wise direction, the measurements covered the primary heat transfer measurement passage, passage 5, and half of the adjacent passages 4 and 6. Spanwise, the measurements started near the endwall,  $z/\text{span} = 0.042$ , and extended to midspan,  $z/\text{span} = 0.50$ . Time mean flow measurements were made with a calibrated 5-hole pitch-yaw probe. Details of the measurement techniques are given by Giel et al. (1996a). Turbulence intensity and integral length scale were measured with a single  $5\ \mu\text{m}$  hot wire. The wire output voltage was calibrated against a density-velocity product in a free air jet; this compensated for the fact that pressure in the rig was lower than atmospheric. Data was recorded at a sampling frequency of 76.2 kHz with an antialiasing filter cutoff frequency of 25.4 kHz. 1048576 data points were recorded for each length scale. The data was analyzed in 32768 blocks with 50% overlap. This resulted in a lowest distinguishable frequency of 2.3 Hz. The resulting 63 autocorrelations were then averaged and the result fit with an exponential curve of the form  $r(t) = \exp(-Ct)$ . Length scale was then computed as  $L_x = U_{avg}/C$  as discussed in Van Fossen et al. (1995).

**Blade Static Pressure Measurements** Surface static pressures were measured using a separate blade set. The two blades forming passage 5 were instrumented with 149 static pressure taps on 9 spanwise planes extending over the entire blade span. Details of the blade static pressure measurements are given by Giel et al. (1996a).

**Heat Transfer Measurements** An array of dots, visible through the liquid crystals, were first painted on the outer surface. Next, two micro-encapsulated chiral nematic liquid crystals with different yellow-band temperatures were mixed and sprayed onto the surfaces, and onto a separate instrumented calibration plate to determine their temperature characteristics. Moffat (1990) showed that micro-encapsulated crystals are less sensitive to illuminating and viewing angles than non-encapsulated crystals. No differences in isotherm location were detected between overlapping photographs.

Two liquid crystals, each with a full color bandwidth of  $\pm 1^\circ\text{C}$ , were used due to surface temperature limits. Low surface temperatures give high uncertainty, and high surface temperatures cause the neoprene to separate from the surface. The higher temperature crystal measured low Stanton number regions and the lower temperature crystal measured high Stanton number regions. For an inlet air temperature of  $18^\circ\text{C}$  ( $65^\circ\text{F}$ ), crystal temperatures of  $38.1^\circ\text{C}$  ( $100.6^\circ\text{F}$ ), and  $48.1^\circ\text{C}$  ( $118.5^\circ\text{F}$ ) were used. In regions where data were available from both crystals, agreement between the crystals verified that the correct definition of Stanton number was used and that the adiabatic wall temperature was reasonably accurate.

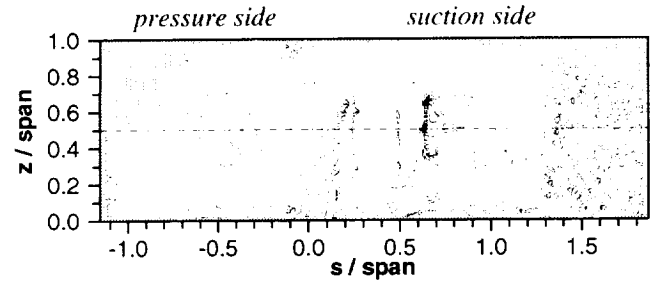


**Fig. 3 Sample digitized liquid crystal data distribution ( $Re_{in} = 0.5 \times 10^6$ ;  $M_{ox} = 1.32$ ; no grid)**

When steady state was achieved, four 35 mm color slide cameras photographed the blade surface. Each camera viewed a subset of the blade surface, with some overlap between camera views. High speed photographic strobes were used to prevent radiative heating of the liquid crystals. The photographic slides were projected onto paper marked with the same dot pattern as on the blades. Slide image dot patterns were aligned with the paper dot patterns. Drawings of the isotherms were made for each camera and crystal temperature. These lines were digitized, with between 2000 to 5000 digitized points for each flow condition. Each point was mapped onto the unwrapped blade coordinates, and the mapping corrected for distortions due to blade curvature. Typically, 20 heater settings covered the full range of surface Stanton numbers. Figure 3 shows a sample digitized data distribution. Gray areas are regions with no available data because of shadowing from other surfaces.

The local surface heat flux,  $q''$ , was corrected for radiative heat transfer loss:

$$q'' = (k/t)(T_{Cu} - T_{lc}) - \epsilon\sigma(T_{lc}^4 - T_{aw}^4)$$

With  $\epsilon = 0.98$ , radiative losses were at most 6% of the net heat flux and typically much less. Variations in the radiative sink temperatures from  $T_{aw}$  to between the exit adiabatic wall temperature and the inlet total temperature produced no significant variations in Stanton numbers. The Stanton number,  $St$ , was defined as follows:

$$St = q'' / \rho_{in} U_{in} C_p (T_{lc} - T_{aw})$$

The local adiabatic wall temperature,  $T_{aw}$ , is:

$$\frac{T_{aw}}{T'_{in}} = r + \frac{1 - r}{1 + 0.5(\gamma - 1)M_{IS}^2}$$

These definitions ensure that the measured Stanton number is independent of liquid crystal temperature. The inlet total temperature,  $T'_{in}$ , was measured by two probes located one axial chord upstream of the blades. The isentropic Mach number,  $M_{IS}$ , was determined from CFD calculations, and a recovery factor of  $r = Pr^{1/3}$  was used everywhere.

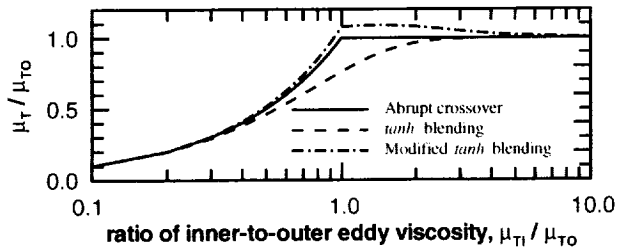


**Fig. 4 Comparison of different blending approaches for turbulent eddy viscosity**

**Uncertainty Analysis** An uncertainty analysis was performed using the method of Kline and McClintock (1953). The major sources of uncertainty are the conductance of the low conductivity layer,  $\delta(k/t)/(k/t) = \pm 5\%$ ; the adiabatic wall temperature,  $\delta T_{aw} = \pm 0.6^\circ\text{C}$  ( $\pm 1.0^\circ\text{F}$ ); the liquid crystal temperature,  $\delta T_{lc} = \pm 0.3^\circ\text{C}$  ( $\pm 0.5^\circ\text{F}$ ); and the copper substrate temperature,  $\delta T_{Cu} = \pm 0.3^\circ\text{C}$  ( $\pm 0.5^\circ\text{F}$ ). The uncertainty in  $T_{aw}$  assumes no uncertainty in the recovery factor,  $r$ , although it is not precisely known as shown by Schlichting (1979). The overall uncertainty in  $St$  was determined to be less than 13%. This maximum uncertainty is in regions of Stanton number less than  $1 \times 10^{-3}$ . For Stanton numbers greater than  $2 \times 10^{-3}$  the uncertainty is less than 8%. Another possible source of bias uncertainty with this method is two-dimensional conduction within the low conductivity layer in regions of high spatial Stanton number gradients. A conduction analysis was performed to examine this error. It was found that the distance from the minimum to the maximum temperature in the region of largest spatial gradient was over 10 times the thickness of the low conductivity layer. A gradient of this magnitude was found to have virtually no adverse impact on the measurements.

## CFD ANALYSIS

To illustrate where analysis improvements are needed, baseline CFD results were done using the three-dimensional Navier-Stokes analysis code, *RV3D*, described by Chima and Yokota (1990) and by Chima (1991). C-type grids were generated using the method of Arnone et al. (1992). Predictions were made using a  $289 \times 49 \times 49$  grid with a near wall spacing,  $y_1^+ < 1$ . A uniform wall temperature was specified.

A two-layer algebraic turbulence model, described by Chima et al. (1993), was used. The *tanh* blending between the inner and outer layers was modified to give better agreement with the data. The turbulent eddy viscosity is given by:  $\mu_t = F \mu_{T0} \tanh(\mu_{T1}/\mu_{T0})$ . Subscripts  $T1$  and  $T0$  refer to the inner and outer layers. In the unmodified blending  $F = 1$ . Since the  $\tanh(1) = 0.76$ , this  $\mu_t$  is less than either the inner or outer value when both are equal. Other formulations, such as the Baldwin-Lomax model rely on an abrupt change between the inner and outer regions. In the modified blending  $F = \sqrt{(1.0 + \min((\mu_{T1}/\mu_{T0})^2, (\mu_{T0}/\mu_{T1})^2))}$ . Figure 4

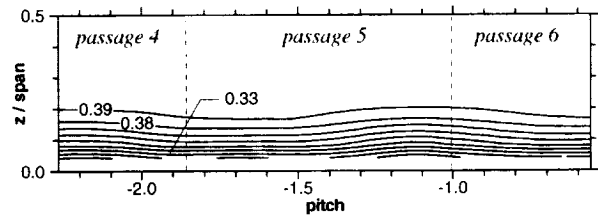


**Fig. 5(a) Inlet Mach numbers without turbulence grid**

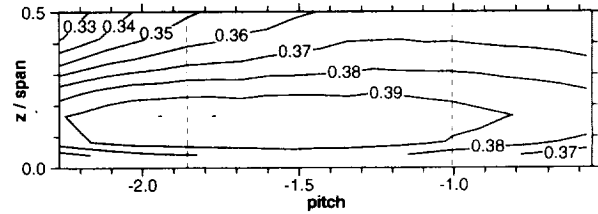


**Fig. 5(b) Inlet Mach numbers with turbulence grid**

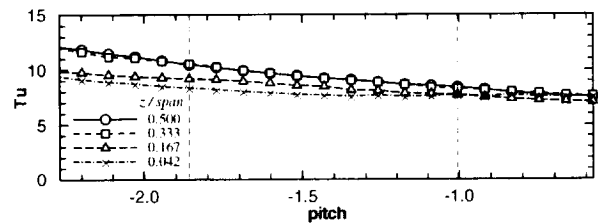


**Fig. 5(c) Inlet turbulence intensity with grid**

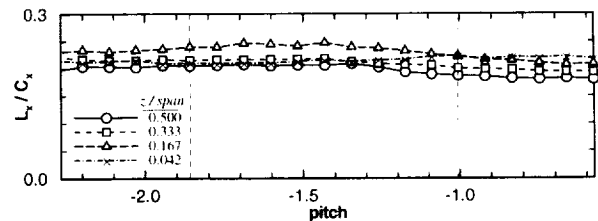


**Fig. 5(d) Inlet turbulence length scale with grid**

compares the original and modified *tanh* blending with an abrupt crossover model. The difference between the modified blending and the abrupt crossover model is small when  $\mu_{T1} < \mu_{T0}$ , the near wall region. However, the modified *tanh* blending is higher after the crossover point, but rapidly returns to the outer layer value.

Transition start was specified using Mayle's (1991) model.  $Tu$  at transition start was the upstream  $Tu$  times the ratio of the upstream velocity to the local isentropic velocity. The transition length model of Boyle and Simon (1998b), an extension of the one by Solomon et al. (1995) to include Mach number effects, was used.

## MEASUREMENT RESULTS

**Inlet Flow Measurements** Inlet mean flow and turbulence quantities measured one axial chord upstream of the blades are shown in Fig. 5. With no turbulence grid in place, the turbulence intensity was spatially uniform with values of 0.5% at  $Re_{in} = 0.5 \times 10^6$  and 0.25% at  $Re_{in} = 1.0 \times 10^6$ .

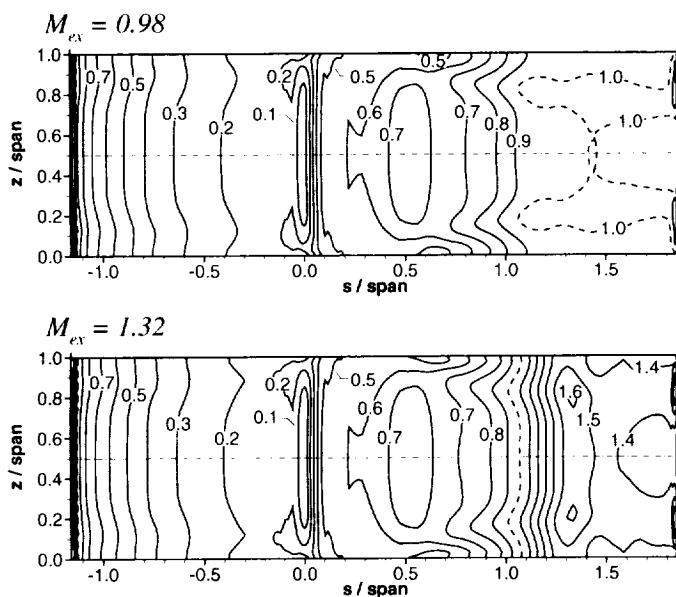


**Fig. 6 Calculated isentropic surface Mach number Blade Static Pressures**

Figure 6 shows calculated isentropic surface Mach number distributions on the unwrapped blade, since blade heat transfer is largely determined by flow features evident in the Mach number distributions. The origin,  $s = 0$ , is the geometric stagnation line at the design inlet flow angle. Giel et al., (1996a) showed that the Mach numbers obtained from the 3D Navier-Stokes code described earlier agreed well with blade loading measurements. The calculated values were used for heat transfer data reduction because they provided significantly better spatial resolution than was available from the experimental data. The surface Mach number distributions were not affected by Reynolds number variations, and their significance will be discussed in conjunction with the heat transfer results.

**Heat Transfer Measurements** Stanton number contours on the unwrapped blade surface are shown in Figs. 7(a) through 7(h). The eight flow conditions are given in Table 2. Exit Mach number variation effects are shown in alternate figures. Grid turbulence effects are seen by comparing alternate pairs of figures. Reynolds number effects are seen by comparing the first four figures to the last four. Regions with no data available are shown as gray areas, and their extent depends on shadows and local heat transfer gradients.

Figure 7(a) shows the Stanton number distribution at  $Re_{in} = 0.5 \times 10^6$ ,  $M_{ex} = 1.32$ , with the turbulence grid. The pressure side shows a relatively flat  $St$  distribution with a minimum above  $3 \times 10^{-3}$ , increasing to  $5 \times 10^{-3}$  near the trailing edge. The stagnation region is evident with a maximum  $St$  over  $6 \times 10^{-3}$ . The Stanton number levels on the suction side of the leading edge initially drop to between  $4 \times 10^{-3}$  and  $5 \times 10^{-3}$ , while those on the pressure surface decrease below  $4 \times 10^{-3}$ . The grid causes

**Table 2 Description of blade heat transfer cases**

Case	$Re_{in}$	$M_{ex}$	$Tu$ grid
1	$0.502 \pm 0.003 \times 10^6$	$1.322 \pm 0.003$	yes
2	$0.500 \pm 0.002 \times 10^6$	$0.985 \pm 0.001$	yes
3	$0.498 \pm 0.005 \times 10^6$	$1.313 \pm 0.003$	no
4	$0.488 \pm 0.001 \times 10^6$	$0.992 \pm 0.001$	no
5	$1.003 \pm 0.007 \times 10^6$	$1.322 \pm 0.001$	yes
6	$1.006 \pm 0.002 \times 10^6$	$0.981 \pm 0.001$	yes
7	$0.999 \pm 0.003 \times 10^6$	$1.314 \pm 0.001$	no
8	$0.989 \pm 0.003 \times 10^6$	$0.998 \pm 0.001$	no

(all repeatabilities based on 95% confidence limits)

early transition, resulting in levels near midspan close to  $St = 5 \times 10^{-3}$ . The decelerating flow region (adverse pressure gradient) evident in Fig. 6 near  $s/span = 0.5$  causes thickening of the turbulent boundary layer, resulting in a minimum  $St$  of  $3 \times 10^{-3}$ . From this point on, the effects of the secondary flows are evident. Many of these effects can be attributed to the vortex structures described by Goldstein and Spores (1988). The passage vortex and the pressure-side leg of the horseshoe vortex now approach the suction surface. Heat transfer is enhanced by the relatively cool secondary flow fluid impinging on the endwall regions of the suction surface. The vortices lift off the endwall and approach midspan. Previous measurements showed the vortices exit the rotor at approximately 25% span. The throat is located at  $s/span = 1.046$  on the suction surface. The supersonic exit flow causes an oblique shock from the trailing edge of the adjacent blade to impinge on the suction surface. The effects of the shock/boundary layer interaction are evident at  $s/span = 1.3$ . The shock impingement causes a thickening of the boundary layer resulting in lower heat transfer. After the shock, secondary flows again cause higher heat transfer rates near the endwall. The Stanton number then decreases as the suction surface boundary layer again grows as the flow approaches the trailing edge.

Figure 7(b) shows the results for Case 2, which differs from the previous one by a reduction in exit Mach number from 1.32 to 0.98. The measurements show, as expected, that the heat transfer on the pressure surface and on the suction surface upstream of the throat are the same for these two cases to within the experimental uncertainty. Downstream of the throat, however, no shock is present to interrupt the suction surface boundary layer and the Stanton number contours continue smoothly to the trailing edge. The secondary flow effects on heat transfer are similar to those observed by Graziani et al. (1980) and by Blair (1994) in the region between the hub and midspan.

Figure 7(c) shows measurements also taken at  $Re_{in} = 0.5 \times 10^6$  and at  $M_{ex} = 1.32$ , but with no inlet turbulence

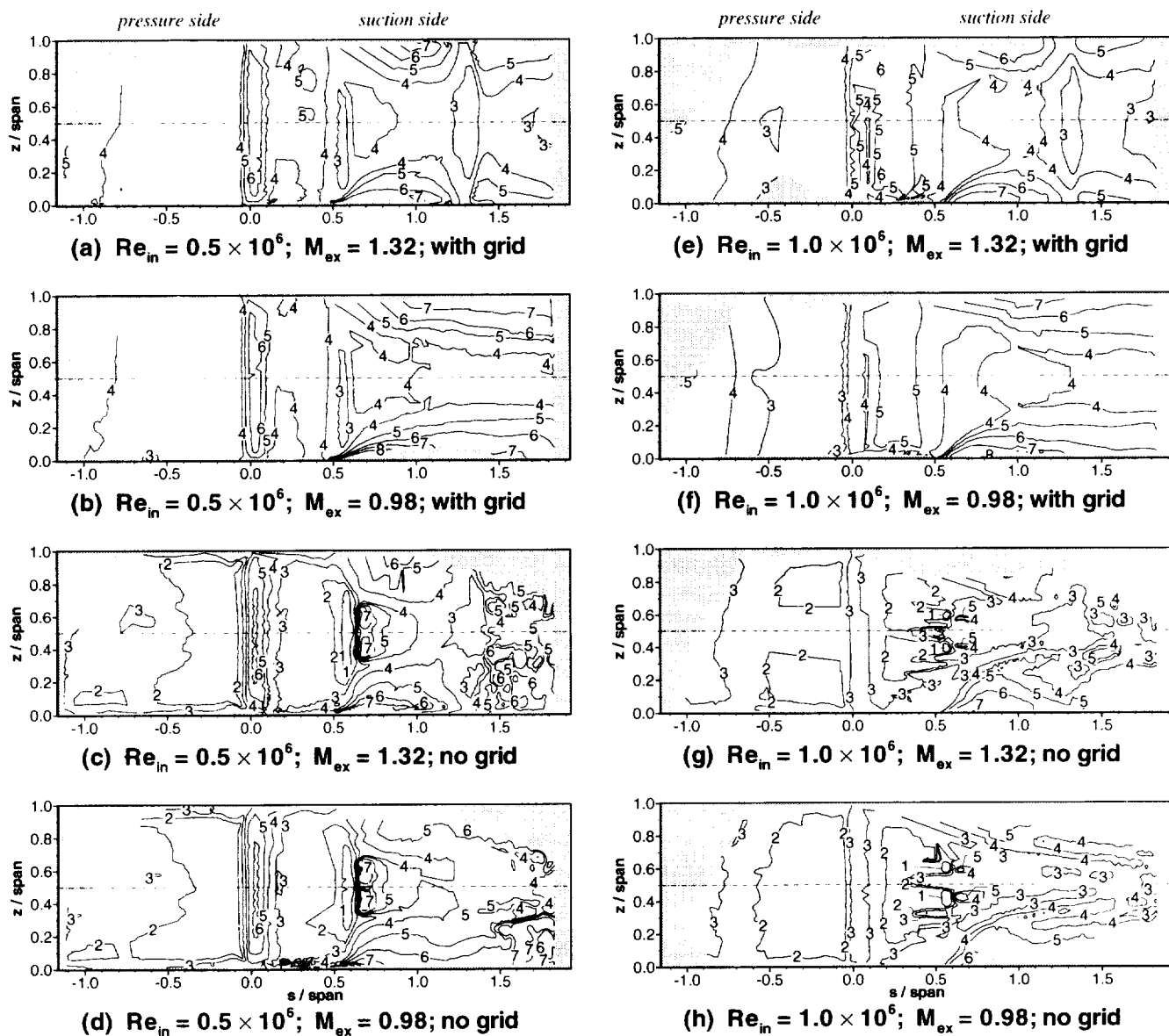


Fig. 7 Measured Stanton number  $\times 1000$

grid. The absence of an upstream grid results in thicker endwall boundary layers, leading to more pronounced secondary flow effects near the pressure surface endwall. Away from the endwalls, Stanton numbers are reduced by one-third to one-half. The pressure surface heat transfer is laminar-like, consistent with low turbulence level and strong favorable pressure gradients. As reported by Baughn et al. (1995), the pressure surface liquid crystal traces were far more nonuniform than those obtained with the grid. The traces had a finger-like appearance.

The width and spanwise extent of the stagnation region contour line of  $St = 6 \times 10^{-3}$  are both reduced over those of Case 1. The width reduction indicates a reduction in the peak heat transfer, as is expected with reduced freestream turbulence. The reduction in spanwise extent

results from the thicker inlet endwall boundary layers.

No transition is observed between the stagnation region and the adverse pressure region on the suction surface. The adverse pressure gradient causes the laminar boundary layer to grow rapidly and to possibly separate. The heat transfer reaches a minimum,  $St < 1 \times 10^{-3}$ , over a significant portion of the span. The induced freestream turbulence from the secondary flows is apparently sufficient to trip the flow near the endwalls thus preventing separation. The flow appears to separate, or to have the characteristics of a very abrupt transition. The transition, or separation combined with a flow reattachment, causes an extremely high gradient in Stanton number. The levels increase from less than  $1 \times 10^{-3}$  to over  $7 \times 10^{-3}$  in a streamwise distance less than one-tenth of the span.

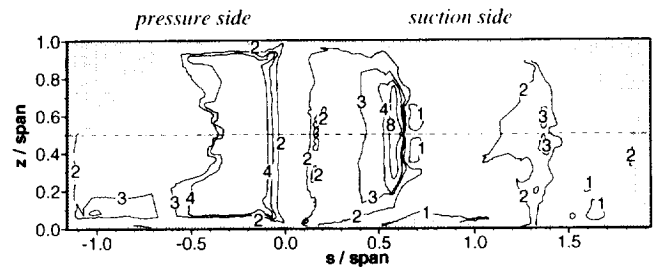
Rivir et al. (1994) observed a similar sharp increase in heat transfer in a reattachment region downstream of a turbulent separation bubble. Further downstream, the Stanton number distribution of this no-grid case looks remarkably like that of the turbulence grid case, Case 1. Downstream of the shock, the levels are again generally in agreement with Case 1, but the distribution is much more distorted. Although the midspan symmetry appears to be quite good, the figure shows that two-dimensional midspan calculations would be inappropriate without accounting for midspan inflow.

Figure 7(d) shows the measurement results for a sonic exit case, Case 4. Again,  $Re_{in} = 0.5 \times 10^6$  with no grid present. Again, there is excellent agreement with the previous supersonic exit case on the pressure surface and on the suction surface upstream of the throat. Downstream of the throat, the contour lines generally follow the streamwise direction but again were more distorted than those of the turbulence grid case.

Figure 7(e) shows the results of the first  $Re_{in} = 1.0 \times 10^6$  case, Case 5. The turbulence grid was installed and the exit was supersonic. Comparing this case to Case 1 shows the effects of increased Reynolds number on heat transfer. The effects are small on the pressure surface because high freestream turbulence gives early transition at either Reynolds number. As expected, the peak stagnation Stanton number is reduced about 20% with increased Reynolds number. Around midspan the high freestream turbulence and high Reynolds number cause very early suction surface transition, and  $St$  levels are hardly reduced from their peak stagnation region levels. The  $St$  levels decrease slightly as the suction surface boundary layer thickens. Because the flow is highly turbulent by this point, the slight adverse pressure gradient near  $s/span = 0.5$  has almost no effect on the heat transfer, and  $St$  levels remain at about  $4 \times 10^{-3}$  until the shock impingement location. The core region following the shock impingement location again appears to be independent of Reynolds number, taking on values of about  $3 \times 10^{-3}$ . Near the endwall the Stanton number levels are nearly independent of Reynolds number. Recall however, that for equivalent Stanton numbers, doubling the Reynolds number doubles the heat transfer coefficient.

The measurement results for this case clearly verify that the blade design objective of more uniform heat transfer rates over the blade surface has been successfully met. Those design objectives are most relevant for this case because the high Reynolds number and the high freestream turbulence levels are most similar to a high pressure turbine rotor operating environment.

Comparing Fig. 7(f) to Fig. 7(e) shows the effects of exit Mach number on the heat transfer for two cases with  $Re_{in} = 1.0 \times 10^6$  and with an inlet turbulence grid.



**Fig. 8 Sample nondimensional surface temperature,  $\theta$  ( $Re_{in} = 0.5 \times 10^6$ ;  $M_{ex} = 1.32$ ; no grid)**

The peak stagnation values for this case were just under  $5 \times 10^{-3}$  while for Case 5 they were just over  $5 \times 10^{-3}$ . The two cases again look very similar on the pressure surface and upstream of the throat on the suction surface. Downstream of the throat, the contour lines again generally follow the streamwise direction.

Figure 7(g) shows the results at  $Re_{in} = 1.0 \times 10^6$ ,  $M_{ex} = 1.32$ , with no turbulence grid. The peak stagnation region Stanton number is just under  $4 \times 10^{-3}$ . The pressure surface is transitional because of the high Reynolds number. Suction surface transition is more complicated than any of the previous cases. At about 30%, 50%, and 70% span, the flow starts to transition just downstream of the stagnation region and continues the transition process relatively slowly. At 40% and 60% span however, the flow remains laminar until it reaches the slight adverse pressure gradient at  $s/span = 0.54$  where it appears to separate, then reattach and become fully turbulent. The behavior at these two discrete spanwise locations resembles that of the entire core region of the  $Re_{in} = 0.5 \times 10^6$ , no grid cases. The most likely cause of the relatively early transition spots was the dots painted on the surface at 33%, 50%, and 67% span at  $s/span = 0.33$ . The dots were barely perceptible to the touch, but the high Reynolds numbers apparently made the boundary layer very sensitive to small disturbances. Following this region, the Stanton number contours again resemble all of the other supersonic exit cases.

Figure 7(h) shows that the pressure surface and the suction surface upstream of the throat again agree very well with the previous supersonic exit case. Downstream of the throat, the Stanton number contours again follow the streamwise direction.

The measurement technique produces a blade surface that is not uniform in either surface temperature or surface heat flux. A sample non-dimensional blade surface temperature,  $\theta$ , is shown in Fig. 8 for the Case 3 which had the largest  $\theta$  variation.  $\theta$  is independent of the particular measurement temperatures and is inversely proportional to the Stanton number, so that boundary conditions for all cases can be found from the Stanton numbers.

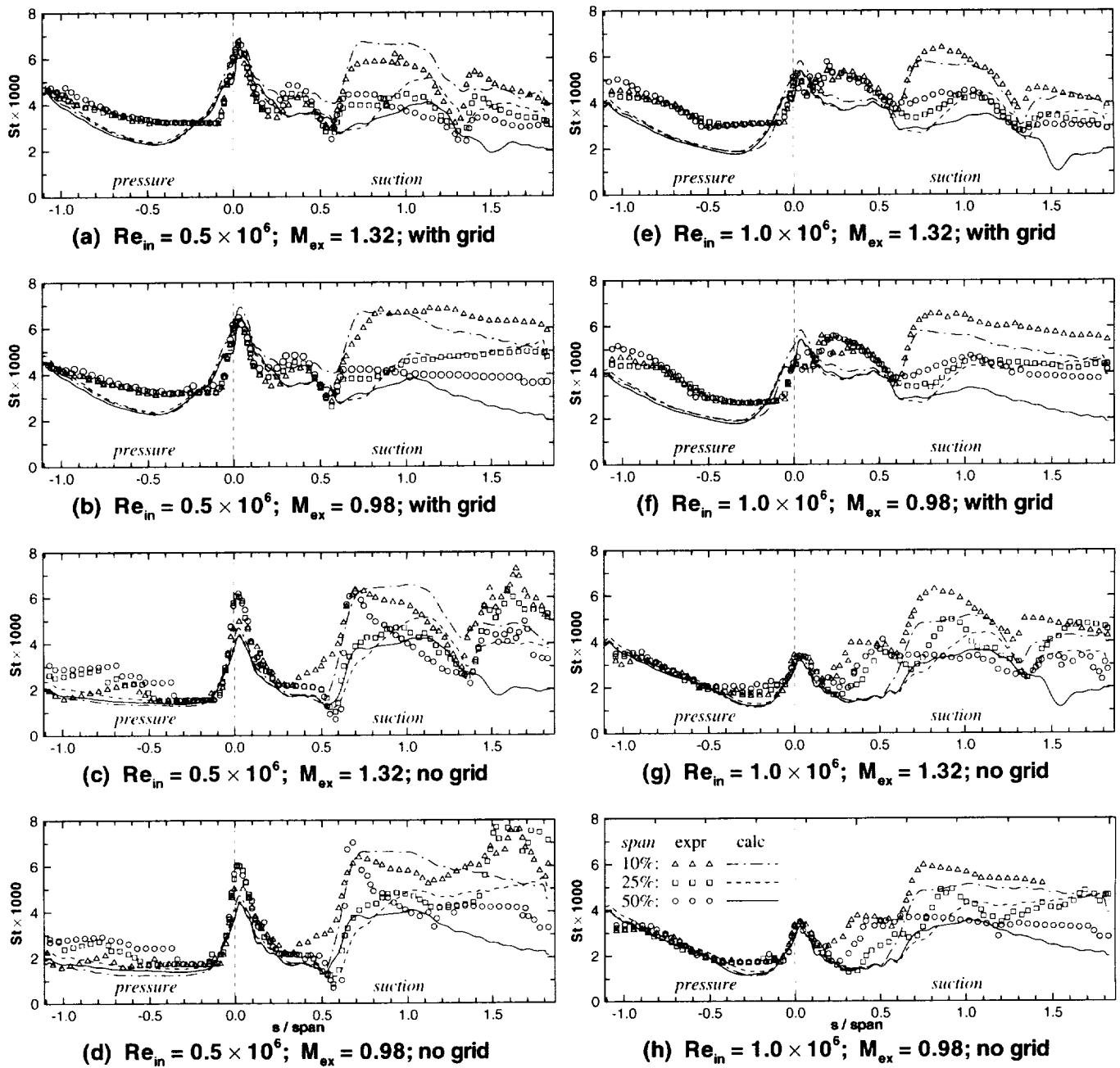


Fig. 9 Measured and predicted Stanton no.  $\times 1000$

An example using Case 3 (Fig. 7c) will now be discussed to relate actual temperatures to values of  $\theta$ . Measurements near the stagnation region with  $T_{lc,2}/T_{in}^* = 1.09$  showed  $St = 6.1 \times 10^{-3}$  and  $\theta = 1.09$ . These measurements required a copper temperature of  $T_{Cu}/T_{in}^* = 1.18$ . Because the copper temperature was essentially uniform, regions of low heat transfer had higher surface temperatures. For example, in the separated flow region the minimum Stanton number was approximately  $0.7 \times 10^{-3}$ .  $\theta$  here was approximately 8.6, resulting in a surface temperature of  $T_{surface}/T_{in}^* = 1.16$ . Had these measurements been made with a uniform heat flux technique, the surface temperature in the low  $St$  region would have been

approximately  $T_{surface}/T_{in}^* = 1.73$ , showing that the present measurement technique produces a thermal boundary condition much closer to a uniform surface temperature than a uniform heat flux.

The liquid crystal Stanton number data were interpolated onto lines at  $z/span = 0.10, 0.25, \text{ and } 0.50$ . Line plots of this data are shown in Figs. 9(a) through 9(h). The contour plots of Fig. 7 show overall trends and spanwise variations, but line plots can be useful for extracting more details of the data. Computational results at the same spanwise locations are also shown in the figures.

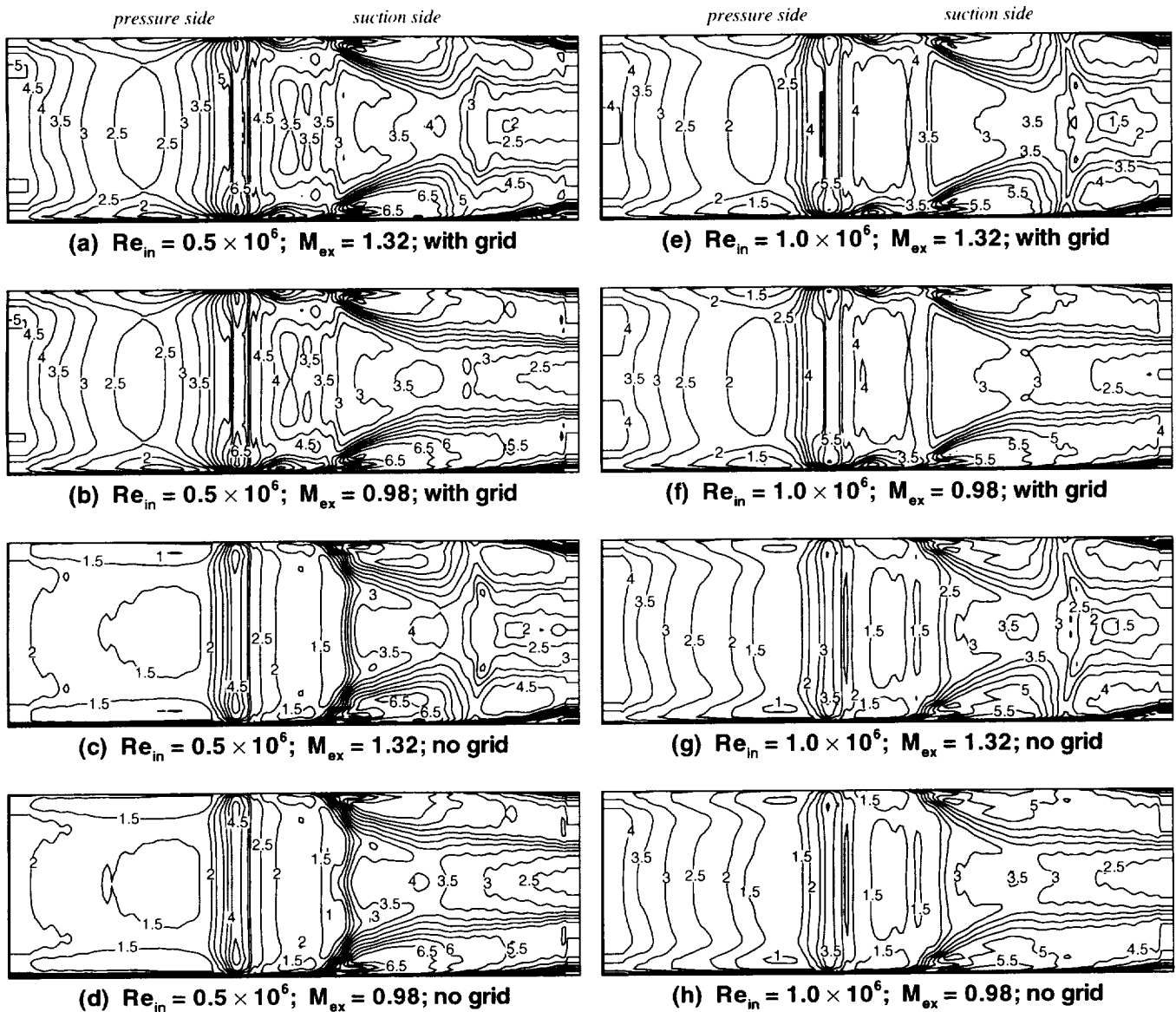


Fig. 10 Predicted Stanton number  $\times 1000$

Some general comments can be made that are common to all of the cases presented above. First, the peak stagnation heat transfer occurs to the suction side of the geometric stagnation line, in contrast to the aerodynamic stagnation line which is slightly towards the pressure surface. Second, Stanton numbers of  $3 \times 10^{-3}$  were observed in the shock impingement region of all supersonic exit cases, regardless of Reynolds number or turbulence grid. Third, secondary flows significantly increase suction surface heat transfer rates near the endwalls. Fourth, the data with the grid in place was smoother than the no-grid data, which was felt to be due to the strong mixing effects of the freestream turbulence. Finally, excellent midspan symmetry is observed.

#### COMPUTATIONAL HEAT TRANSFER

The predicted heat transfer rates are shown in Figs. 10(a) through 10(h) in the same order as the experimental data. The analysis assumed midspan symmetry, but full span solutions are shown for comparisons with data. An inlet  $Tu = 8\%$  was used for predictions with the grid installed, and  $Tu = 1\%$  for the no grid cases.

**Low Reynolds number comparisons** Figure 10(a) shows results for  $Re_{in} = 0.5 \times 10^6$ ,  $M_{ex} = 1.32$ , and with the grid. In the analysis, the turbulence intensity affected start of transition and gave increased laminar region heat transfer. Leading edge and nearby suction surface heat transfer are well predicted. The analysis and data both show suction surface minimums near  $s/span = 0.5$ . The minimum experimental Stanton number in this region is

$3 \times 10^{-3}$ . At  $s/\text{span} = 0.5$  predictions show a region at this level, and a minimum at  $2.5 \times 10^{-3}$  close to one quarter span. The midspan peak Stanton number of  $4 \times 10^{-3}$  is downstream of the experimental peak, indicating the transition length is overpredicted. However, overall the agreement with the data in the transition region is good. At  $s/\text{span} = 0.5$  a high heat transfer region forms near the endwall. This region expands downstream consistent with the data. The peak experimental Stanton number is  $7 \times 10^{-3}$ , while the peak predicted value is  $6.5 \times 10^{-3}$ . Heat transfer behavior in this region is due to secondary flows as discussed by Goldstein et al. (1995), and is not just due to cross channel flows passing over the unheated endwall. An analysis with the blade and endwall both heated showed blade heat transfer very similar to the predictions. The effect of the shock on the heat transfer is clearly seen, as it was in the data. After the shock, the predicted midspan heat transfer decreases, but this is not seen in the data. Close to the endwalls both the analysis and the data show regions of increased heat transfer after the shock. The peak computed value in this region is  $4.5 \times 10^{-3}$ , while the peak data value was  $5 \times 10^{-3}$ .

Both the computations and experiment show a very rapid decrease in pressure surface heat transfer away from the leading edge. The minimum experimental contour level is  $4 \times 10^{-3}$ , and encompasses nearly two thirds of the pressure surface. The absolute minimum measured pressure surface Stanton number was close to  $3 \times 10^{-3}$ . Except close to the endwall, the minimum predicted Stanton number is  $2.5 \times 10^{-3}$ . Transition was predicted to begin at close to 30% of the surface distance, and was not complete until after 50% of the surface distance. Underpredicting the minimum Stanton number appears to imply a poor start of transition prediction. However, if the analysis underpredicted the effects of freestream turbulence on the pressure surface heat transfer, it would also underpredict the heat transfer, even if the start and length of transition were correctly predicted. Close to the endwall at 40% of the pressure surface distance a region of low heat transfer is predicted, but is not seen in the data. At close to 90% of the surface distance there are Stanton number levels of  $5 \times 10^{-3}$  in both the experimental and computational contours.

Figure 10(b) shows predictions for the lower exit Mach number case. A change in heat transfer is only seen from the throat region to the trailing edge of the suction surface. At this lower Mach number there is little evidence that the much weaker shock affects the heat transfer. Over the last 40% of the suction surface the Stanton number lines are nearly horizontal. This location is governed by the cascade aspect ratio. The cascade symmetry forces the secondary and vortex flows to stop moving closer to midspan at some chordwise loca-

tion. Close to midspan the analysis shows lower than measured heat transfer. In addition to a deficiency in the turbulence modeling, the analysis could be overpredicting the amount of secondary flows forced into the midspan region, giving a thicker boundary layer and reduced heat transfer.

Figure 10(c) shows heat transfer levels on the pressure surface, and the suction surface prior to transition, are affected when the grid is absent. The pressure surface heat transfer is much lower at the 1% inlet  $Tu$  level. At the leading edge the midspan Stanton number is slightly less than  $4.5 \times 10^{-3}$ . This corresponds to a Frossling number,  $Nu_d/\sqrt{Re_c}$ , of 1.04. The experimental leading edge Frossling number is higher, 1.39. There is no mechanism for the model to augment the heat transfer at low turbulence intensity, so the analysis gives the same result as laminar flow at the stagnation point of a cylinder. The calculations predicted laminar flow on the pressure surface. In the experimental data there is a large pressure surface area enclosed within the  $St = 2 \times 10^{-3}$  contour. In the calculations there is a minimum contour of  $1.5 \times 10^{-3}$  and at midspan it extends into the region where the experimental data show increased heat transfer. Closer to the pressure surface trailing edge the experimental Stanton number level is  $3 \times 10^{-3}$ , while the calculated value is only  $2 \times 10^{-3}$ . These results indicate that there is a mechanism increasing the pressure surface heat transfer that the analysis does not account for.

Suction surface heat transfer also differs between the high and low  $Tu$  cases due to turbulence modifying the transition start location. Data show a minimum Stanton number contour of  $1 \times 10^{-3}$ . The prediction shows a minimum contour level of  $1.5 \times 10^{-3}$ , enclosing a somewhat larger area. The start of transition is accurately predicted. Prior to transition, the suction surface of the blade shows the same relative behavior as the pressure surface. In these laminar regions the predicted heat transfer is lower than the data.

In the midspan region, after the minimum suction surface heat transfer, the predicted heat transfer shows a much lower peak than the data. These differences may be due to flow separation and reattachment, rather than transition. The analysis predicted a low shear value at the start of transition, and a very short transition region caused by the adverse pressure gradient. If the actual transition was slightly later than predicted, separation would have occurred. Very high heat transfer is expected at reattachment. The experimental heat transfer shows two small contour areas above and below midspan at a level of  $St = 7 \times 10^{-3}$ . The analysis showed a contour level in the same region between  $3.5 \times 10^{-3}$  and  $4.0 \times 10^{-3}$ . The algebraic turbulence model used did not correctly predict the heat transfer in this region, and improved

turbulence models should give better agreement. Calculations were done with the wall temperatures varying in the same manner as that shown in Fig. 8, but did not improve the agreement with data.

The increased near-endwall heat transfer due to secondary flows is very similar to the no grid case, and is well predicted. The peak predicted Stanton number is  $6.5 \times 10^{-3}$ , while the peak measured value is  $7 \times 10^{-3}$ . The behavior in the shock impingement region is also well predicted. Both data and predictions show contour levels of  $3 \times 10^{-3}$ . Downstream of the shock, near midspan, the data show Stanton number levels above  $4 \times 10^{-3}$ . The prediction shows a decrease in heat transfer towards the trailing edge. This behavior is similar to that for the corresponding high  $Tu$  case. Away from midspan the grid case data show a higher average heat transfer level, and a more chaotic distribution. The analysis, however, shows similar behavior but at a slightly lower level. The surface pressure distributions were the same for the high and low  $Tu$  analyses. There was no mechanism in the analysis that would account for higher freestream turbulence after the flow was fully turbulent.

Figure 10(d) shows that decreasing Mach number from 1.32 to 0.98 for the no grid case resulted in changes similar to those for the same Mach number change at the high  $Tu$  grid case.

**High Reynolds number comparisons** The primary effect of increasing the Reynolds number by a factor of two on the heat transfer distribution is to change the transition location. Prior to transition the Stanton number is expected to decrease by  $\sqrt{2}$  when the Reynolds number is doubled. For fully turbulent flow the Stanton number is expected to decrease by 13% when the Reynolds number is doubled, assuming  $St \propto Re^{-0.2}$ .

The first comparison is between the two Reynolds numbers at  $M_{ex} = 1.32$  and the grid installed. Figure 10(e) shows that downstream of the leading edge on the suction surface the Stanton number is higher for the higher Reynolds number, as it is in the data. This is due to transition moving forward at the higher  $Re$ . The leading edge heat transfer decreases only by about 15%. However, this is consistent with the high turbulence intensity and high  $Re_d$ . The correlation of Van Fossen et al. (1995) predicts a 26% reduction in  $St$  due to the change in Reynolds number. However, the correlation also predicts that at higher Frossling numbers, seen in the data, the effect of a Reynolds number variation is less. Elsewhere on the blade, the change in Stanton number is as expected. The flow is turbulent, and there is a decrease of 10-20% in the Stanton number when the Reynolds number is doubled.

Comparing Figs. 10(e) and 10(f) shows the same heat transfer changes at the high Reynolds number for a Mach number change as were seen at the low Reynolds number. Overall, the agreement with the data is good. However, again the predictions show too low a heat transfer on the suction surface midspan region downstream of the throat.

Figure 10(g) shows that, with no grid in place, instead of decreased  $St$  when  $Re$  doubles, the Stanton number more than doubles near the pressure surface trailing edge. This is due to transition. At the lower Reynolds number, pressure surface transition did not occur. At the higher Reynolds number transition was predicted to begin near 30% of pressure surface distance, and end at 60% of the surface distance. This is consistent with the experimental data, although the change in  $St$  is not as dramatic in the data. Suction surface transition was predicted to occur at nearly the same location for both Reynolds numbers. Prior to transition the lower Reynolds number had a region between  $St = 1.5$  and  $2 \times 10^{-3}$ . For the higher Reynolds number the same region shows Stanton numbers less than  $1.5 \times 10^{-3}$ . This is consistent with what one would expect for laminar flow. Figure 10(h) shows that the change in Stanton number with decreased Mach number is the same at both Reynolds numbers.

Overall the analysis underpredicts the heat transfer, which may be partly due to differences in the manner in which the heat transfer coefficient was defined. For consistency with the experimental data the Stanton numbers are based on the wall heat flux divided by the difference between the wall temperature and the adiabatic wall temperature. The same adiabatic wall temperature distribution was used to determine the experimental and computational Stanton numbers. Therefore, differences are due to differences in the wall heat flux. Calculations were done with different wall temperatures. From the resultant heat fluxes the adiabatic wall temperature was calculated for each grid point on the blade surface. The recovery factor determined from the Navier-Stokes analysis was closer to unity than the recovery factor used to calculate the Stanton numbers. The recovery factor was also greater than most of the recovery factors given by Schlichting (1979). If the inlet total temperature was used to calculate Stanton numbers instead of the local adiabatic wall temperature, predicted Stanton numbers would be up to 40% higher. Differences arising from differences in the recovery factor only help to explain differences in the suction surface heat transfer. Only heat transfer in high Mach number regions is affected by variations in the recovery factor.

## SUMMARY AND CONCLUSIONS

The primary effect of a factor of two variation in Reynolds number was to move the transition locations. For the low inlet turbulence intensity cases, flow on the suction surface remained laminar up to an adverse pressure gradient region. Subsequently, the Stanton number rose rapidly to a high level. At low  $Tu$ , pressure surface transition was observed at high, but not at low, Reynolds numbers. The shock in the supersonic exit cases impinged on the suction surface, where measurements and calculations showed Stanton number levels of  $3 \times 10^{-3}$  independent of Reynolds number and turbulence grid. The subsonic cases showed Stanton number contours generally following the expected streamlines and remaining unchanged after the throat. The data showed that the turbulence grid increased leading edge heat transfer and moved the transition locations forward. For the high Reynolds number and turbulence grid case the suction surface transition moved almost to the stagnation point.

Even with high turbulence the midspan leading edge heat transfer did not greatly exceed that seen elsewhere along midspan. The good spatial resolution due to the large scale and the liquid crystal technique allowed the secondary flow effects to be clearly quantified.

Comparing computational and experimental results illustrated regions of good agreement and regions where modeling improvements are needed. Transition was well predicted, as were the effects of secondary flows on the suction surface heat transfer. High heat transfer in the near endwall region was well predicted. The leading edge heat transfer was well predicted for the high turbulence intensity cases, but was underpredicted for the low turbulence intensity cases. For the low Reynolds number, no grid cases, the analysis predicted a very short suction surface transition region, due to an adverse pressure gradient. Experimentally, the laminar flow may have separated and reattached rather than smoothly transitioned, which may be the reason that the analysis underpredicted the heat transfer. The analysis also underpredicted the heat transfer near midspan downstream of the throat on the suction surface. This could be due to turbulence model deficiencies, or an overprediction of the amount of fluid forced into the midspan region by secondary flows. The latter would cause the calculated midspan boundary layer to be thicker than the experimental one, leading to lower heat transfer.

The blade heat transfer data presented here, the end-wall heat transfer data of Giel et al. (1998), along with the aerodynamic data of Giel et al. (1996a) comprise a complete set of data for CFD code and model validation.

Electronic data tabulations for all eight cases, including raw digitized data to allow contour plotting at any level, are available upon request.

## REFERENCES

- Arnone, A., Liou, M.-S. and Povinelli, L. A., 1992, "Navier-Stokes Solution of Transonic Cascade Flows Using Non-Periodic C-Type Grids," *AIAA Journal of Propulsion and Power*, Vol. 8, No. 2, pp. 410-417.
- Arts, T., Duboue, J.-M., and Rollin, G., 1997, "Aero-Thermal Performance Measurements and Analysis of a Two-Dimensional High Turning Rotor Blade," ASME paper 97-GT-120.
- Baughn, J. W., Butler, R. J., Byerley, A. R., and Rivir, R. B., 1995, "An Experimental Investigation of Heat Transfer, Transition and Separation on Turbine Blades at Low Reynolds Number and High Turbulence Intensity," ASME paper 95-WA/HT-25.
- Blair, M. F., 1994, "An Experimental Study of Heat Transfer in a Large-Scale Turbine Rotor Passage," *ASME Journal of Turbomachinery*, Vol. 116, No. 1, pp. 1-13.
- Boyle, R. J., Lucci, B. L., Verhoff, V. G., Camperchioli, W. P., and La, H., 1998a, "Aerodynamics of a Transitioning Turbine Stator Over a Range of Reynolds Numbers," ASME paper 98-GT-285.
- Boyle, R. J., and Simon, F. F., 1998b, "Mach Number Effects on Turbine Blade Transition Length Prediction," ASME paper 98-GT-367.
- Chima, R. V., and Yokota, J. W., 1990, "Numerical Analysis of Three-Dimensional Viscous Internal Flows," *AIAA Journal*, Vol. 28, No. 5, pp. 798-806.
- Chima, R. V., 1991, "Viscous Three-Dimensional Calculations of Transonic Fan Performance," AGARD Propulsion and Energetics Symposium on Computational Fluid Mechanics for Propulsion, San Antonio, Texas, May 27-31.
- Chima, R. V., Giel, P. W., and Boyle, R. J., 1993, "An Algebraic Turbulence Model for Three-Dimensional Viscous Flows," AIAA paper 93-0083, (NASA TM-105931).
- Civinskas, K. C., Boyle, R. J., and McConnaughey, H. V., 1990, "Turbine Blading Designed for High Heat Load Space Propulsion Applications," *AIAA Journal of Propulsion and Power*, Vol. 6, pp. 598-611.
- Dunn, M. G., Kim, J., Civinskas, K. C., and Boyle, R. J., 1994, "Time-Averaged Heat Transfer and Pressure Measurements and Comparison with Predictions for a Two-Stage Turbine," *ASME Journal of Turbomachinery*, Vol. 116, pp. 14-23.

- Giel, P. W., Thurman, D. R., Lopez, I., Boyle, R. J., Van Fossen, G. J., Jett, T. J., Camperchioli, W. P., and La, H., 1996a, "Three-Dimensional Flow Field Measurements in a Transonic Turbine Cascade," ASME paper 96-GT-113, presented at the ASME International Gas Turbine Conference, Birmingham, England, June 10-13.
- Giel, P. W., Sirbaugh, J. R., Lopez, I., and Van Fossen, G. J., 1996b, "Three-Dimensional Navier-Stokes Analysis and Redesign of an Imbedded Bellmouth Nozzle in a Turbine Cascade Inlet Section," ASME *Journal of Turbomachinery*, Vol. 118, No. 3, pp. 529-535.
- Giel, P. W., Thurman, D. R., Van Fossen, G. J., Hippensteele, S. A., and Boyle, R. J., 1998, "Endwall Heat Transfer Measurements in a Transonic Turbine Cascade," ASME *Journal of Turbomachinery*, Vol. 120, No. 2, pp. 305-313.
- Goldstein, R. J., and Spores, R. A., 1988, "Turbulent Transport on the Endwall in the Region Between Adjacent Turbine Blades," ASME *Journal of Heat Transfer*, Vol. 110, No. 4, pp. 862-869.
- Goldstein, R. J., Wang, H. P., and Jabbari, M. Y., 1995, "The Influence of Secondary Flows Near the Endwall and Boundary Layer Disturbance on Convective Transport From a Turbine Blade," ASME *Journal of Turbomachinery*, Vol. 117, No. 4, pp. 657-665.
- Graziani, R. A., Blair, M. F., Taylor, R. J., and Mayle, R. E., 1980, "An Experimental Study of Endwall and Airfoil Surface Heat Transfer in a Large Scale Turbine Blade Cascade," ASME *Journal of Engineering for Power*, Vol. 102, No. 2, pp. 1-11.
- Guenette, G. R., Epstein, A. H., Giles, M. B., Haines, R., and Norton, R. J. G., 1989, "Fully Scaled Transonic Turbine Rotor Heat Transfer Measurements," ASME *Journal of Turbomachinery*, Vol. 111, No. 1, pp. 1-7.
- Hippensteele, S. A., Russell, L. M., and Torres, F. J., 1988, "Local Heat-Transfer Measurements on a Large Scale-Model Turbine Blade Airfoil Using a Composite of a Heater Element and Liquid Crystals," ASME *Journal of Engineering for Gas Turbines and Power*, Vol. 107, pp. 953-960.
- Joslyn, D., and Dring, R., 1992, "Three-Dimensional Flow in an Axial Turbine: Part 1 - Aerodynamic Mechanisms," ASME *Journal of Turbomachinery*, Vol. 114, No. 1, pp. 61-70.
- Kline, S. J., and McClintock, F. A., 1953, "Describing Uncertainty in Single-Sample Experiments," *Mechanical Engineering*, Vol. 75, Jan., pp. 3-8.
- Martinez-Botas, R. F., Lock, G. D., and Jones, T. V., 1994, "Heat Transfer Measurements in an Annular Cascade of Transonic Gas Turbine Blades Using the Transient Liquid Crystal Technique," ASME 94-GT-172.
- Mayle, R. E., 1991, "The Role of Laminar-Turbulent Transition in Gas Turbine Engines," ASME *Journal of Turbomachinery*, Vol. 113, pp. 509-537.
- Moffat, R. J., 1990, "Experimental Heat Transfer," *Proc. of the Ninth Int'l Heat Transfer Conf.*, Jerusalem, Israel, Vol. 1, pp. 187-205.
- Rivir, R. B., Johnston, J. P., and Eaton, J. K., 1994, "Heat Transfer on a Flat Surface Under a Region of Turbulent Separation," ASME *Journal of Turbomachinery*, Vol. 116, No. 1, pp. 57-62.
- Schlichting, H., 1979, *Boundary-Layer Theory*, Seventh Edition, McGraw-Hill, New York, p. 714.
- Solomon, W. J., Walker, G. J., and Gostelow, J. P., 1995, "Transition Length Prediction For Flows With Rapidly Changing Pressure Gradients," ASME paper 95-GT-241.
- Thulin, R. D., Howe, D. C., and Singer, I. D., 1982, "Energy Efficient Engine - High-Pressure Turbine Detailed Design Report," NASA CR-165608.
- Van Fossen, G. J., Simoneau, R. J., and Ching, C. Y., 1995, "Influence of Turbulence Parameters, Reynolds Number, and Body Shape on Stagnation-Region Heat Transfer," ASME *Journal of Heat Transfer*, Vol. 117, pp. 597-603.
- Verhoff, V. G., Camperchioli, W. P., and Lopez, I., 1992, "Transonic Turbine Blade Cascade Testing Facility," AIAA Paper No. 92-4034, NASA TM-105646.

# REPORT DOCUMENTATION PAGE

Form Approved  
OMB No. 0704-0188

Public reporting burden for this collection of information is estimated to average 1 hour per response, including the time for reviewing instructions, searching existing data sources, gathering and maintaining the data needed, and completing and reviewing the collection of information. Send comments regarding this burden estimate or any other aspect of this collection of information, including suggestions for reducing this burden, to Washington Headquarters Services, Directorate for Information Operations and Reports, 1215 Jefferson Davis Highway, Suite 1204, Arlington, VA 22202-4302, and to the Office of Management and Budget, Paperwork Reduction Project (0704-0188), Washington, DC 20503.

<b>1. AGENCY USE ONLY</b> (Leave blank)		<b>2. REPORT DATE</b> August 1999	<b>3. REPORT TYPE AND DATES COVERED</b> Technical Memorandum	
<b>4. TITLE AND SUBTITLE</b>  Blade Heat Transfer Measurements and Predictions in a Transonic Turbine Cascade			<b>5. FUNDING NUMBERS</b>  WU-523-26-13-00 1L161102AH45 NAS3-98008	
<b>6. AUTHOR(S)</b>  P.W. Giel, G.J. Van Fossen, R.J. Boyle, D.R. Thurman and K.C. Civinskas				
<b>7. PERFORMING ORGANIZATION NAME(S) AND ADDRESS(ES)</b>  NASA Glenn Research Center Cleveland, Ohio 44135-3191 and U.S. Army Research Laboratory Cleveland, Ohio 44135-3191			<b>8. PERFORMING ORGANIZATION REPORT NUMBER</b>  E-11775	
<b>9. SPONSORING/MONITORING AGENCY NAME(S) AND ADDRESS(ES)</b>  National Aeronautics and Space Administration Washington, DC 20546-0001 and U.S. Army Research Laboratory Adelphi, Maryland 20783-1145			<b>10. SPONSORING/MONITORING AGENCY REPORT NUMBER</b>  NASA TM-1999-209296 ARL-TR-2029	
<b>11. SUPPLEMENTARY NOTES</b> Prepared for the 1999 International Gas Turbine and Aeroengine Congress cosponsored by the American Society of Mechanical Engineers and the International Gas Turbine Institute, Indianapolis, Indiana, June 7-10, 1999. P.W. Giel, Dynacs Engineering Company, Inc., Brook Park, Ohio; (work funded under NASA Contract NAS3-98008); G.J. VanFossen and R.J. Boyle, NASA Glenn Research Center; D.R. Thurman and R.C. Civinskas, U.S. Army Research Laboratory, NASA Glenn Research Center. Responsible person, R.J. Boyle, organization code 5820, (216) 433-5889.				
<b>12a. DISTRIBUTION/AVAILABILITY STATEMENT</b>  Unclassified - Unlimited Subject Categories: 02, 07 and 34  This publication is available from the NASA Center for AeroSpace Information, (301) 621-0390.			<b>12b. DISTRIBUTION CODE</b>  Distribution: Nonstandard	
<b>13. ABSTRACT</b> (Maximum 200 words)  Detailed heat transfer measurements and predictions are given for a turbine rotor with 136° of turning and an axial chord of 12.7 cm. Data were obtained for inlet Reynolds numbers of 0.5 and 1.0×10 <sup>6</sup> , for isentropic exit Mach numbers of 1.0 and 1.3, and for inlet turbulence intensities of 0.25% and 7.0%. Measurements were made in a linear cascade having a highly three-dimensional flow field resulting from thick inlet boundary layers. The purpose of the work is to provide benchmark quality data for three-dimensional CFD code and model verification. Data were obtained by a steady-state technique using a heated, isothermal blade. Heat fluxes were determined from a calibrated resistance layer in conjunction with a surface temperature measured by calibrated liquid crystals. The results show the effects of strong secondary vortical flows, laminar-to-turbulent transition, shock impingement, and increased inlet turbulence on the surface heat transfer.				
<b>14. SUBJECT TERMS</b> Gas turbines; Heat transfer; Transonic flow; Supersonic turbines; Cascade wind tunnel; Liquid crystals; Turbomachinery; Turbulent heat transfer; Convective heat transfer; Stanton number			<b>15. NUMBER OF PAGES</b> 21	
			<b>16. PRICE CODE</b> A03	
<b>17. SECURITY CLASSIFICATION OF REPORT</b> Unclassified	<b>18. SECURITY CLASSIFICATION OF THIS PAGE</b> Unclassified	<b>19. SECURITY CLASSIFICATION OF ABSTRACT</b> Unclassified	<b>20. LIMITATION OF ABSTRACT</b>	